

Optical and Magnetic Properties of Manganese-Incorporated Zinc Sulfide Nanorods Synthesized by a Solvothermal Process

Subhajit Biswas, Soumitra Kar, and Subhadra Chaudhuri*

Department of Materials Science, Indian Association for the Cultivation of Science, Kolkata 700 032, India

Received: June 10, 2005; In Final Form: July 26, 2005

Manganese-incorporated ZnS ($\text{Mn}_x\text{Zn}_{1-x}\text{S}$) nanorods were synthesized by a simple solvothermal process. Synthesized nanorods were single crystalline. Manganese incorporation in the ZnS lattice induces a phase transformation from hexagonal wurtzite to cubic zinc blende structure. The diameter of the nanorods increased with the increase of Mn concentration. Intense orange luminescence at ~ 585 nm was observed for the nanorods. Six-line hyperfine splitting was observed in the EPR spectra for lower Mn concentrations, whereas broad Lorentzian-shaped EPR spectra were obtained for higher Mn concentrations because of the Mn–Mn cluster formation at higher Mn concentrations.

1. Introduction

Zinc sulfide, a II–VI group compound semiconductor, is particularly suitable for use as host material for a large variety of dopants because of its wide band gap (3.75 eV).¹ It has been extensively studied for a variety of applications, e.g., in optical coatings, solid-state solar window layers, electrooptic modulators, photoconductors, field effect transistors, optical sensors, photocatalysts, electroluminescent materials, phosphors, and other light-emitting materials. In fact, ZnS has found special importance in thin-film electroluminescent devices, lasers, and flat-panel displays when doped with divalent manganese ions.^{2–6} Manganese usually occupies substitutional sites in the Zn lattice as a divalent ion, and the excitation and decay of this ion produces an orange luminescence at approximately 590 nm.^{7,8} This emission peak is generally associated with a transition between $^4\text{T}_1$ and $^6\text{A}_1$ energy levels. Also, electron paramagnetic resonance (EPR) technique has been widely used to obtain an insight about the local crystal field effects and symmetry around Mn^{2+} ions.⁹ The observed Mn^{2+} spectral features were used to explain the changes in the optical properties of the material. Manganese-doped ZnS nanoparticles have been synthesized by using laser ablation, MBE, MOCVD, certain physical methods, solution growth, and other different chemical techniques.^{10–14}

Keeping in mind the recent interest of one-dimensional nanostructure,^{15–17} we have synthesized Mn-incorporated ZnS nanorods with varying Mn concentration in powder form via a solvothermal process. To our knowledge, there are no reports on the synthesis of Mn^{2+} -incorporated ZnS nanorods via wet chemical methods. In this study, the photoluminescence (PL) and electron paramagnetic resonance (EPR) properties of $\text{Mn}_x\text{Zn}_{1-x}\text{S}$ nanorods are reported. The dependence of these properties upon Mn concentration is presented.

2. Experimental Section

For the synthesis of $\text{Mn}_x\text{Zn}_{1-x}\text{S}$ nanorods, a Teflon-lined stainless steel cylindrical closed chamber with 100 mL capacity was used. All the chemicals were of analytical grade and were

used without any further purification. The x -value was varied within 0–0.2. Appropriate amounts of zinc nitrate ($\text{Zn}(\text{NO}_3)_2 \cdot 6\text{H}_2\text{O}$), manganese acetate [$(\text{CH}_3\text{COO})_2\text{Mn} \cdot 4\text{H}_2\text{O}$], and thiourea (NH_2CSNH_2) were placed in the Teflon lined chamber, which was then filled with an ethylenediamine (en)–water mixture (in 1:1 volume ratio) up to 80% of its volume. Thiourea was used in 3 times the stoichiometric ratio. After 30 min of stirring, the closed chamber was placed inside a box furnace at a preset temperature of 200 °C for 12 h and then cooled to room temperature naturally. The resulting white precipitate was filtered off and washed several times in water and ethanol. The final product was dried in a vacuum at 80 °C for 6 h to get a white powder.

The products were analyzed using an X-ray diffractometer (XRD, Seifert 3000P) with $\text{Cu K}\alpha$ radiation, and the compositional analysis was done by energy-dispersive X-ray (EDAX, Kevex, Delta class I). Microstructures and crystal structures of the nanorods were obtained using transmission electron microscopic (TEM) and high-resolution TEM (HRTEM, JEOL 2010) studies. Photoluminescence (PL) measurements were carried out at room temperature, using 335 nm as the excitation wavelength, with a luminescence spectrometer (Perkin-Elmer, LS50B). Electron paramagnetic resonance study of the powder sample was done with Varian E–109C X-band spectrometer.

3. Results and Discussion

Ethylenediamine (en) was found to promote one-dimensional growth of CdS by a solvothermal process due to its chelating property.¹⁸ But ZnS nanorods could not be synthesized with ethylenediamine by following the same experimental conditions used for the CdS nanorods. Instead, flakes such as the two-dimensional complex $\text{ZnS} \cdot (\text{NH}_2\text{CH}_2\text{CH}_2\text{NH}_2)_{0.5}$ were produced.¹⁹ The differences in the coordination ability of ethylenediamine with Zn^{2+} and Cd^{2+} ions and some other kinetic factors related to the solvothermal growth might be the reason behind the difference.¹⁹ However, by annealing this complex precursor in Ar atmosphere at high temperature or by treating the complex hydrothermally, a mixture of pure hexagonal ZnS nanorods and particles could be obtained. It was observed that, by mixing water with the ethylenediamine (en) in equal volume ratio, uniform hexagonal ZnS nanorods were produced at 200

* Corresponding author. E-mail: mssc2@mahendra.iacs.res.in. Telephone: 091-033-2473-4971. Fax: +91-033-2473-2805.

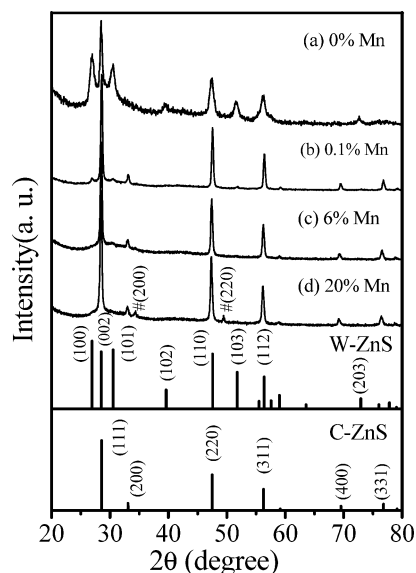


Figure 1. XRD spectra of the $\text{Mn}_x\text{Zn}_{1-x}\text{S}$ nanorods. Standard results for the hexagonal wurtzite and cubic zinc blende structure of ZnS are also shown.

$^{\circ}\text{C}$. The hexagonal phase of ZnS is stable at temperatures higher than 1020°C , and the cubic phase of ZnS is stable below this temperature. However, the presence of the chelating solvent at high pressure might have brought down the free energy difference between the hexagonal and cubic phases of ZnS, resulting in the formation of wurtzite ZnS at a lower temperature than expected. The same experimental conditions were used for the fabrication of $\text{Mn}_x\text{Zn}_{1-x}\text{S}$ nanorods.

The crystal structure and phase of the powder products were investigated through XRD. Figure 1 shows few representative XRD patterns of the $\text{Mn}_x\text{Zn}_{1-x}\text{S}$ nanorods. The XRD spectra revealed that undoped ZnS nanorods were crystallized with a pure hexagonal wurtzite structure. The most interesting observation from the XRD spectra was the transformation of the crystal structure of the products from hexagonal to cubic, with Mn incorporation in the ZnS nanorods. The XRD spectra revealed that the incorporation of Mn^{2+} ions even in a minute (0.05%) quantity introduced a phase transformation from hexagonal to cubic. However, some tiny peaks due to the hexagonal phase were still present (Figure 1b) for lower Mn concentrations (<6%). With the increase of Mn concentration, the peaks due to the wurtzite phase disappeared, and only peaks due to phase-pure cubic ZnS with zinc blende structure were detected from the XRD patterns (Figure 1c–d). At sufficiently high Mn concentration ($\sim 20\%$ Mn), two small peaks at 34.3° and 49.2° due to (200) and (220) planes of stable α -MnS with a rock salt structure appeared in the XRD spectra. MnS cluster formation at a higher Mn value was further confirmed by adding 40 atom % of Mn, and the resulting products showed strong XRD peaks due to α -MnS along with the ZnS phase. From the results, it seems that the incorporated Mn^{2+} ions preferred the cubic phase of ZnS as the host lattice. As the ionic radius of Mn^{2+} is about 10% larger than that of the Zn^{2+} ion, the substitution has forced a small change in the site symmetry and that might be the reason behind the phase transformation of ZnS with Mn incorporation. The growth and morphology of the crystals in a solvothermal process were controlled by the solubility of the precursors in the particular solvent at the synthesis temperature. Also, it was reported that wurtzite ZnS nanocrystals can be transformed to the sphalerite (cubic) phase in the presence of some organic molecules.²⁰ Actually, in the presence of the organic salt, the free energy difference between the hexagonal and cubic phase

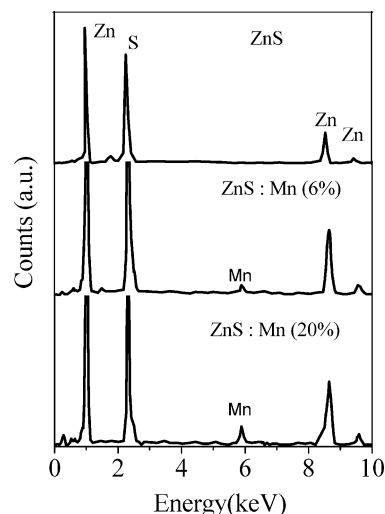


Figure 2. EDAX spectra of the $\text{Mn}_x\text{Zn}_{1-x}\text{S}$ nanorods.

might have increased again toward their normal value, and as a result, the cubic phase gets favored over the hexagonal phase. So the presence of the organic Mn salt (manganese acetate $[(\text{CH}_3\text{COO})_2\text{Mn}\cdot 4\text{H}_2\text{O}]$) could be another reason for the phase transformation of the $\text{Mn}_x\text{Zn}_{1-x}\text{S}$ nanorods.

The compositional analysis of the $\text{Mn}_x\text{Zn}_{1-x}\text{S}$ nanostructures was performed by EDAX analysis. Three representative EDAX spectra of the $\text{Mn}_x\text{Zn}_{1-x}\text{S}$ nanorods are shown in Figure 2. In pure ZnS, elemental Zn and S were found in a near-stoichiometric ratio with little sulfur deficiency. In the Mn-doped ZnS samples, the amount of Mn detected by EDAX analysis was much less than those actually added during synthesis. For example, only 0.24, 2.49, and 5.58 atom % Mn was detected for 1, 6, and 20% doped ZnS nanorods, respectively.

The microstructures of the $\text{Mn}_x\text{Zn}_{1-x}\text{S}$ nanostructures were studied through TEM images. Figure 3a, c, and e show the TEM images of the ZnS, $\text{Mn}_{0.01}\text{Zn}_{0.99}\text{S}$, and $\text{Mn}_{0.2}\text{Zn}_{0.8}\text{S}$ nanorods, respectively. The diameters and lengths of the undoped ZnS nanorods varied within 12–15 nm and 100–200 nm, respectively. With incorporation of Mn in the ZnS, the width of these nanorods increased gradually and became ~ 100 nm for 20% Mn-doped ZnS nanorods, while the length remained almost unchanged. The exact mechanism behind the increase of width of the nanorods with the Mn concentration was not clear and needs further study. However, this increase in width could be ascribed to the presence of the organic Mn salt and the subsequent phase transformation. Solubility of the precursors and the ease of displacement of the anions in the solvent were crucial factors in determining the size of the nanoforms, and presence of the organic salt might have increased the overall solubility and the ionic dissociation of the precursors, resulting in the rapid growth and increase in the width of the nanorods.

The crystal structures of these $\text{Mn}_x\text{Zn}_{1-x}\text{S}$ nanorods were further studied through HRTEM images. Figure 3b shows the HRTEM image of a single undoped ZnS nanorod with lattice spacing 3.13 \AA , corresponding to the (002) plane of wurtzite ZnS. The arrows on both sides of the image indicate the boundary as well as the growth direction (002) of the nanorods. The growth direction of the ZnS nanorod was further confirmed to be (002) from the SAED pattern shown in the inset of Figure 3b. Figure 3d shows the HRTEM image of 1% Mn-doped ZnS nanorods. The spacing of the lattice fringes in the HRTEM image was 3.12 \AA , which was the measured lattice spacing for the undoped ZnS nanorods (Figure 3b), but close observations revealed that, unlike the undoped nanorods, the crystal structure

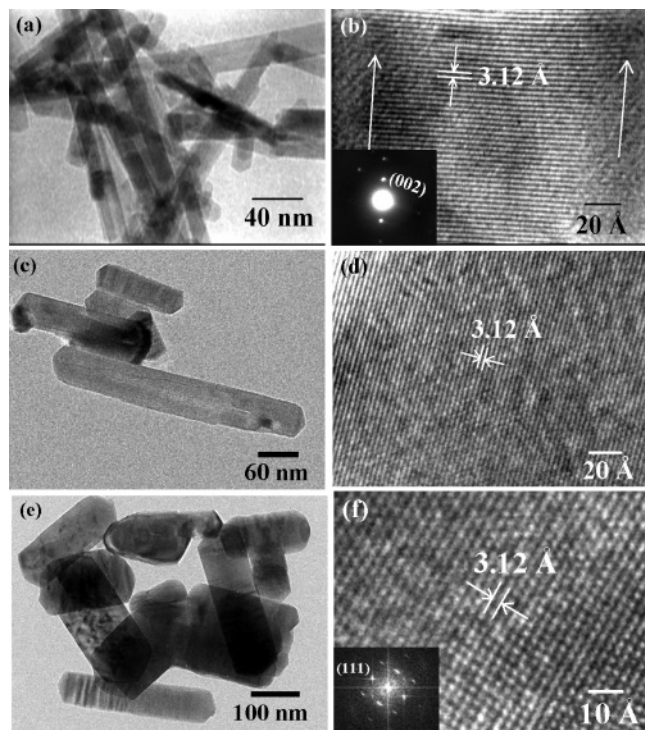


Figure 3. TEM image of the (a) Pure ZnS nanorods, (c) $\text{Mn}_{0.01}\text{Zn}_{0.99}\text{S}$ nanorods, and (e) $\text{Mn}_{0.2}\text{Zn}_{0.8}\text{S}$ nanorods. HRTEM image of the (b) ZnS nanorod along with the SAED pattern in its inset, (d) $\text{Mn}_{0.01}\text{Zn}_{0.99}\text{S}$ nanorod, and (f) $\text{Mn}_{0.2}\text{Zn}_{0.8}\text{S}$ nanorod along with the corresponding FFT pattern in the inset.

for the doped nanorod was that of cubic ZnS. The lattice fringes in the 1% Mn-doped ZnS nanorod were due to the (111) plane of cubic ZnS. The growth direction of the nanorod was perpendicular to the lattice fringes, i.e., (111). The same kind of cubic ZnS structure was also detected for the 20% Mn-incorporated ZnS nanorods. This (111) plane was also the growth direction for the 20% Mn-incorporated cubic ZnS nanorods. This is also confirmed from the FFT pattern of the HRTEM image, as shown in the inset of Figure 3f. Despite the presence of the tiny peaks due to the rock salt MnS in the XRD pattern of the 20% Mn-incorporated ZnS nanorods, no lattice patterns corresponding to cubic MnS were observed. This could be attributed to the fact that MnS might have formed as some small clusters within the ZnS host lattice in some local vacancy sites without disturbing the ZnS lattice as a whole.

Room-temperature photoluminescence spectra of the $\text{Mn}_x\text{Zn}_{1-x}\text{S}$ nanorods measured with a 335 nm excitation wavelength are shown in Figure 4. Photoluminescence spectra recorded for the undoped ZnS nanorods (plot a) showed two emission bands, one blue emission band at ~ 400 nm and another green band at ~ 500 nm. The blue emission band was associated with the recombination of free charge carriers at defect sites, possibly at surface of the nanostructures.^{21,22} The green band at ~ 500 nm was most likely due to the self-activated defect centers formed by the zinc vacancy inside the lattice.^{4,23} For the doped ZnS nanorods, an additional strong orange emission at 585 nm was observed along with the above-mentioned emissions. Interestingly, the intensity of the blue emission at 400 nm remains almost unaltered with incorporation of Mn into the ZnS host lattice, confirming our assumption that the blue emission was due to surface defect states. Otherwise, the phase transformation of the products with the incorporation of the Mn ions into the ZnS lattice should have an effect on the emission. However, the intensity of the green (500 nm) and the orange

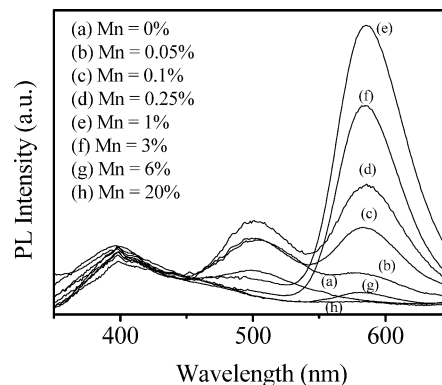


Figure 4. Room-temperature photoluminescence spectra of the $\text{Mn}_x\text{Zn}_{1-x}\text{S}$ nanorods.

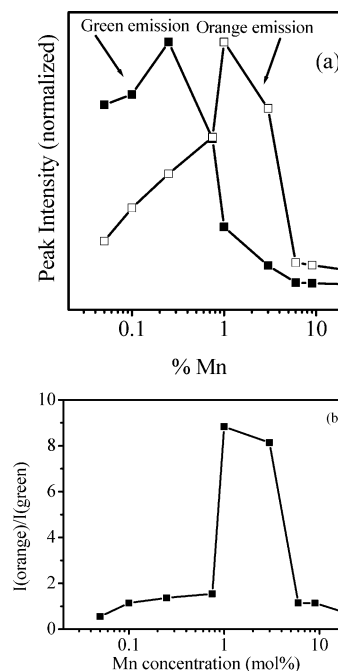


Figure 5. (a) Variation of the intensity of the green and orange emissions with atomic % of Mn. Intensity of the two peaks was normalized. (b) Actual intensity ratio of the orange to green emissions vs atomic % of Mn.

(585 nm) bands first increased and then decreased with the increase of Mn concentrations. The nature of the variation of the intensity of the green and orange emissions at 500 and 585 nm, respectively, with the concentration of Mn^{2+} are shown in Figure 5a. The intensity of the 500 nm peak attained its maximum at 0.25% Mn incorporation and almost disappeared for 3% Mn incorporation, while the orange emission was at maximum for 1%, decreased appreciably for $\sim 6\%$, and finally, completely disappeared for 20% of Mn. This unusual behavior of the green emission at 500 nm with Mn incorporation indicates the fact that its origin could be zinc-vacancy-related defect states. As ionic radius of Mn^{2+} is 10% larger than that of the Zn^{2+} ion, the initial incorporation of a minute quantity of Mn into the ZnS lattice and subsequent transformation from the hexagonal to the cubic phase might have activated the defect sites, resulting in the increased intensity of the peak. Further addition of the Mn^{2+} ion should have substituted the Zn vacancy sites, resulting in the reduction of the intensity of this peak due to quenching of self-activated centers. Another reason behind the quenching of the Zn-vacancy-related green emission is that, because of the relatively long lifetime of the green luminescence at ~ 500 nm, the radiative decay cannot compete with the

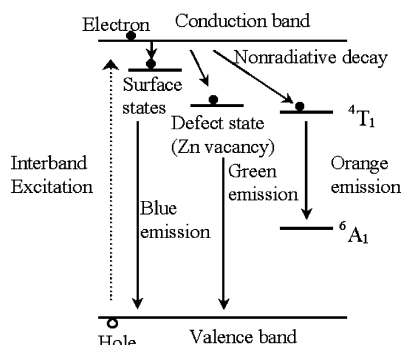


Figure 6. Schematic representation of the model ascribed to different emission from the $\text{Mn}_x\text{Zn}_{1-x}\text{S}$ nanorods.

nonradiative energy transfer to Mn^{2+} , whereas the short lifetime of the blue emission allows it to compete with the energy transfer to Mn^{2+} and thus still persists in the PL spectrum. The PL peak at around 585 nm was due to an indirect excitation. The origin of this orange emission can be attributed to the $4T_1-6A_1$ transition of the Mn^{2+} .⁷ The initial increase in the intensity of the peak with Mn^{2+} concentration (up to 1%) was due to the formation of more and more Mn^{2+} luminescent centers, whereas the quenching of the orange luminescence at higher Mn concentration was due to the interaction of the neighboring Mn^{2+} ions at the nearest, the second nearest, and probably at the third nearest neighbor sites. To understand the quantum efficiency of the Mn^{2+} luminescence, a plot of the ratio of intensity of orange to green emission with the Mn concentration is shown in Figure 5b. The plot indicated high quantum efficiency for Mn^{2+} luminescence for 1% Mn incorporation. The sharp fall in the plot within the region of 3–6% Mn-incorporated samples can be attributed to the strong Mn–Mn exchange interaction for those samples. According to the energy transfer model proposed by Tanaka²⁴ and Chen et al.,²⁵ the energy transfer is most likely from the ZnS band edge or the recombination of carriers localized at Mn^{2+} ions. The excited charge carriers can decay nonradiatively to the ZnS surface states with emission in the blue region, or to the Mn^{2+} 3D states, where Mn^{2+} d–d transition leads to the orange emission. The relative intensity of the orange and blue emission depends on the transition probabilities of the various steps involved and Mn^{2+} ion concentration. Here, we have modified the above-mentioned model for better understanding of the origins of all the emissions observed in the Mn-incorporated ZnS nanorods. The representative schematic diagram of the model is shown in Figure 6.

The embedding of Mn inside the matrix is also inferred from EPR measurements. Because the hyperfine splitting constants depend on the environment of Mn ions, the bonding characteristics between Mn ions and the host lattice can be explained by EPR analysis. The Mn^{2+} charge state has a half filled d shell ($3d^5$) with angular momentum $L = 0$ and spin $S = 5/2$. The distinctive feature of EPR of Mn is its hyperfine splitting arising from the ^{55}Mn nucleus ($I = 5/2$). Here, the spin Hamiltonian can be written as

$$H = g\beta\mathbf{H}\cdot\mathbf{S} + |A|\mathbf{S}\cdot\mathbf{I} + \frac{1}{6}a(S_x^4 + S_y^4 + S_z^4) + D[S_z^2 - \frac{1}{3}S(S+1)]$$

Here, β is the Bohr magneton, H is the applied magnetic field, and g , D , and $|A|$ are the EPR parameters. The first term in the equation is due to Zeeman interaction, the second to hyperfine interaction with the Mn nucleus, the third due to cubic field, and the fourth due to fine structure splitting. Figure 7 shows the EPR spectra of the representative $\text{Mn}_x\text{Zn}_{1-x}\text{S}$ nanorods.

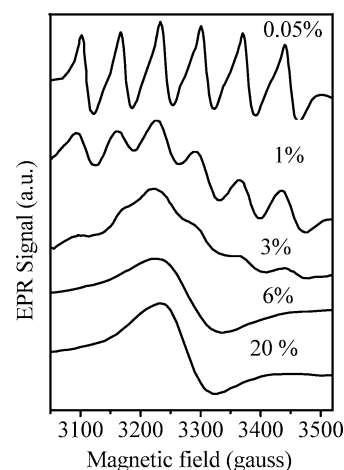


Figure 7. EPR spectra of the $\text{Mn}_x\text{Zn}_{1-x}\text{S}$ nanorods.

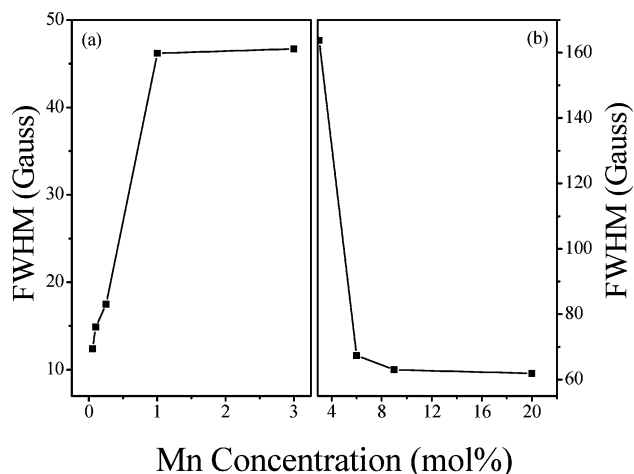


Figure 8. Variation of fwhm with Mn concentration for (a) single Mn^{2+} ion and (b) Mn clusters.

Typical six-line hyperfine structures appeared at the lower concentration of Mn. At very low Mn concentration, this spectral feature aroused due to $|{-1/2}\rangle$ to $|1/2\rangle$ transition coupled to Mn nuclear spin ($I = 5/2$) as few Mn^{2+} ions isolated from each other were distributed inside the ZnS nanorod lattice. But for $\text{Mn}_x\text{Zn}_{1-x}\text{S}$ samples with x values 0.01 and 0.03, the typical EPR spectra (Figure 7) represented two kinds of Mn^{2+} centers. One component of the spectra was due to Mn^{2+} ions and had six hyperfine lines, whereas the other was due to formation of small Mn clusters, resulting in a broad resonance line. At higher Mn concentrations, the density of Mn^{2+} ions introduced within the ZnS nanorod lattice increased to such a value that they started interacting with each other, and the resulting Mn–Mn interaction started influencing the EPR results. For more than 3% Mn incorporation in ZnS nanorods, a single Lorentzian-shaped spectrum was obtained. This broad line can be attributed to clustered manganese ions, which strongly influence one another through their magnetic moments. The sharp drop in photoluminescence intensity for the 6% Mn-doped sample (Figure 4) could be explained with the help of EPR results. The extensive broadening of the EPR spectrum for the 6% sample was attributed to enhanced Mn–Mn coupling, which was the cause of the quenching of the PL intensity at that Mn concentration as stated earlier.

The variation of full width half-maximum (fwhm) for the spectrum of a single ion and a Mn cluster is shown in Figure 8a and b, respectively. The line width for the single ion increased with the increase of Mn content in ZnS. This broadening with

the incorporation of Mn^{2+} was due to magnetic dipole–dipole interaction. Here, hyperfine interaction was much stronger than the exchange interaction. However, with the increase in Mn concentrations, the exchange interaction became much more dominant, and the hyperfine lines merged together, giving a single broad line. In case of the Mn cluster, fwhm decreased with the increase in Mn concentration (Figure 8b). Here, exchange interaction becomes much stronger than hyperfine splitting, and because of the exchange-narrowing effect between Mn^{2+} ions, the variation in the broadening was visible. Unlike the observation of Sapra et al.⁸ (for the Mn-doped ZnS nanoclusters), our EPR and PL results were quite consistent with each other. The orange emission of our samples was maximum for 1 atom % Mn, and subsequently, it quenched with further addition of Mn, indicating Mn–Mn interaction taking place at a higher Mn value. This was well supported by the EPR spectra showing that exchange interaction started dominating from 3% Mn. However, Sapra et al. reported maximum orange emission for 9% Mn, whereas their EPR spectra suggest Mn–Mn exchange interaction was quite dominating well below that amount.

4. Conclusion

Manganese-incorporated ZnS nanorods were synthesized via a solvothermal process. The sample without Mn corresponds to hexagonal ZnS. Mn^{2+} ion incorporation into the ZnS nanorods resulted in morphological as well as structural changes. The diameter of the ZnS nanorods increased gradually from 12–15 nm to ~100 nm for 0–20% Mn incorporations. Manganese incorporation introduces a phase transformation from wurtzite to cubic structure. Three different emissions in the blue, green, and orange regions were visible in the room-temperature photoluminescence spectra. These blue, green, and orange emissions were attributed to the surface defects, zinc-vacancy-related self-activated defect sites, and $^4\text{T}_1$ – $^6\text{A}_1$ transition of the Mn^{2+} ions, respectively. Quenching of the orange emission at higher Mn concentrations was attributed to Mn–Mn dipolar interaction. The isolated Mn^{2+} ion and Mn cluster was also detected from the EPR measurement. EPR results support the presence of magnetic dipole interaction for the Mn-incorporated ZnS nanorods with a higher Mn concentration. Also, the basic

advantage of our approach is that a bulk amount of the nanorods can be prepared at low temperature without using any kind of template. These powder samples containing single crystalline nanorods with very good emission properties could be utilized to fabricate emissive devices.

References and Notes

- (1) Sooklal, K.; Cullum, B. S.; Angel, S. M.; Murphy, C. J. *J. Phys. Chem.* **1996**, *100*, 4551.
- (2) Garlick, G. F. J.; Gibson, A. F. *J. Opt. Soc. Am.* **1949**, *39*, 935.
- (3) McClean, I. P.; Thomas, C. B. *Semicond. Sci. Technol.* **1992**, *7*, 1394.
- (4) Falcony, C.; Garcia, M.; Ortiz, A.; Alonso, J. C. *J. Appl. Phys.* **1992**, *72*, 1525.
- (5) Tang, W.; Cameron, D. C. *Thin Solid Films* **1996**, *280*, 221.
- (6) Bredol, M.; Merikhi, J. *J. Mater. Sci.* **1998**, *33*, 471.
- (7) Bhargava, R. N.; Gallagher, D.; Hong, X.; Nurmikko, A. *Phys. Rev. Lett.* **1994**, *72*, 416.
- (8) Sapra, S.; Nanda, J.; Anand, A.; Bhat, S. V.; Sarma, D. D. *J. Nanosci. Nanotechnol.* **2003**, *3*, 392.
- (9) Borse, P. H.; Srinivas, D.; Shinde, R. F.; Date, S. K.; Vogel, W.; Kulkarni, S. K. *Phys. Rev. B* **1999**, *60*, 8659.
- (10) Soo, Y. L.; Ming, Z. H.; Huang, S. W.; Kao, Y. H.; Bhargava, R. N.; Gallagher, D. *Phys. Rev. B* **1994**, *50*, 7602.
- (11) Yang, H.; Wang, Z.; Song, L.; Zhao, M.; Chen, Y.; Dou, K.; Yu, J.; Wang, L.; *Mater. Chem. Phys.* **1997**, *47*, 249.
- (12) Dinsmore, A. D.; Hsu, D. S.; Qadri, S. B.; Cross, J. O.; Kennedy, T. A.; Gray, H. F.; Ratna, B. R. *J. Appl. Phys.* **2000**, *88*, 4985.
- (13) Yang, H.; Holloway, P. H.; Ratna, B. B. *J. Appl. Phys.* **2003**, *93*, 586.
- (14) Yeung, K. M.; Tsang, W. S.; Mak, C. L.; Wong, K. H. *J. Appl. Phys.* **2002**, *92*, 3636.
- (15) Frank, S.; Poncharal, P.; Wang, Z. L.; Heer, W. A. *Science* **1998**, *280*, 1744.
- (16) Heath, J. R.; Kuekes, P. J.; Snider, G. S.; Williams, R. S. *Science* **1998**, *280*, 1716.
- (17) Hu, J.; Ouyang, M.; Yang, P.; Lieber, C. M. *Nature* **1999**, *399*, 48.
- (18) Li, Y. D.; Liao, H. W.; Ding, Y.; Qian, Y. T.; Yang, L.; Zhou, G. E. *Chem. Mater.* **1998**, *10*, 2301.
- (19) Deng, Z. X.; Wang, C.; Sun, X. M.; Li, Y. D. *Inorg. Chem.* **2002**, *41*, 869.
- (20) Murakoshi, K.; Hosokawa, H.; Tanaka, N.; Saito, M.; Wada, Y.; Sakata, T.; Mori, H.; Yanagida, S. *Chem. Commun.* **1998**, 321.
- (21) Bol, A. A.; Meijerink, A. *Phys. Rev. B* **1998**, *58*, R15997.
- (22) Kar, S.; Chaudhuri, S. *J. Phys. Chem. B* **2005**, *109*, 3298.
- (23) Samelson, H.; Lempicki, A. *Phys. Rev.* **1962**, *125*, 901.
- (24) Tanaka, M. *J. Lumin.* **2002**, *100*, 163.
- (25) Chen, W.; Su, F.; Li, G.; Joly, A. G.; Malm, J. O.; Bovin, J. O. *J. Appl. Phys.* **2002**, *92*, 1950.